Distribution and Burgers vectors of dislocations in semiconductor wafers investigated by rocking-curve imaging

Daniel Lübbert,[a]*‡ Claudio Ferrari,[b] Petr Mikulík,[c,d] Petra Pernot,[c,e] Lukas Helfen,[c,e] Nicola Verdi,[b] Dušan Korytár[c,f] and Tilo Baumbach[c]

[a]HASYLAB/DESY, Notkestr. 85, D-22607 Hamburg, Germany, [b]MASPEC/IMEM-CNR, Parco Area delle Scienze 37/A, Fontanini, I-43010 Parma, Italy, [c]EADQ, Fraunhofer-IZfP, Krügerstr. 22, D-01326 Dresden, Germany, [d]Institute of Condensed Matter Physics, Faculty of Science, Masaryk University, Kotlářská 2, CZ-61137 Brno, Czech Republic, [e]European Synchrotron Radiation Facility, 6 rue Jules Horovitz, F-38043 Grenoble, France, and [f]Institute of Electrical Engineering, SAS, Vrbovská cesta 110, SK-92101 Piešťany, Slovakia. Correspondence e-mail: daniel.luebbert@gmx.de

The method called 'rocking-curve imaging' (RCI) has recently been developed to visualize lattice imperfections in large crystals such as semiconductor wafers with high spatial resolution. The method is based on a combination of X-ray rocking-curve analysis and digital X-ray diffraction topography. In this article, an extension of the method is proposed by which dislocation densities in large-scale samples (semiconductor wafer crystals) can be quantified and their variation across the sample surface determined in an instrumentally simple way. Results from a nearly dislocation-free S-doped InP crystal and a semi-insulating GaAs are presented; both display a clearly non-random distribution of dislocations.

1. Introduction

A variety of methods and instrumental setups have been developed in recent years to monitor crystalline perfection, mosaicity and grain structure of single crystals and/or poly-crystals using X-rays.

Classically, there are two kinds of X-ray methods available to investigate the crystalline quality of a sample. X-ray diffractometry, working in reciprocal space, reaches very high angular resolution and is thus highly sensitive to lattice distortions. However, it usually averages over the real-space dimensions of the sample (millimetres). X-ray diffraction topography, on the other hand, is a real-space imaging method that investigates the spatial distribution of defects in a crystal with spatial resolution of down to 1 μm. In its standard forms, it cannot easily be used, however, to obtain quantitative information on angular quantities (lattice misorientation *etc.*). Both methods were invented many decades ago [see DuMond (1937) and Zachariasen (1945) for diffractometry, and Berg (1931) and Lang (1959) for topography], and have developed into very well established techniques [for recent reviews see *e.g.* Bowen & Tanner (1998) and Authier (2001)].

Various approaches have emerged in recent years that allow both spatial and angular information on lattice imperfections

to be obtained simultaneously. Starting from diffractometry with laboratory X-ray tubes, the incident-beam size can be restricted by slits, and local rocking curves measured by scanning over the sample surface. Entire semiconductor wafers have been mapped out in this way (Goorsky *et al.*, 1997; Ferrari *et al.*, 1997), and appropriate equipment is now available commercially. However, the best achievable resolution is of the order of millimetres, making it impossible to correlate the measured macroscopic sample properties with their microscopic causes.

At synchrotron radiation sources, the high flux, good collimation and small source size of the X-ray beam allow much smaller beam spot sizes to be used in such investigations, in particular when focusing the (white or monochromatic) beam with highly sophisticated X-ray optics (Castelnau *et al.*, 2001; Larson *et al.*, 2002; Tamura *et al.*, 2003).

These setups have been used to quantify dislocation densities in steel *via* the width of local rocking curves (Castelnau *et al.*, 2001), to map grain structure and orientation in polycrystalline aluminium (Larson *et al.*, 2002), as well as to investigate electromigration damage in Cu and Al interconnect lines for microelectronics (Tamura *et al.*, 2003).

A slightly different approach is followed by Poulsen *et al.* in the method referred to as '3D-XRD' (Poulsen *et al.*, 2001; Poulsen & Schmidt, 2003). By using a one-dimensionally focused beam, recording diffraction patterns at several

‡ Now at: Humboldt-Universität zu Berlin, Institut für Physik, Newtonstr. 15, D-12489 Berlin, Germany.

different sample–detector distances and analyzing the data in a ray-tracing procedure, they determine the grain structure of polycrystals in three dimensions.

An inherent disadvantage of all the above methods is that they are slow, since they need to scan successively a microbeam over the sample area and/or to make the same measurement at a number of different sample–detector distances. As a fundamental alternative, several groups developed early versions of what may be summarized as multi-exposure X-ray topography (Chikaura & Suzuki, 1993; Köhler, 1993). These imaging methods, using a very wide (rather than micro-) X-ray beam and an area detector, profited greatly from the increasing availability of electronic area detectors (CCD cameras). Thus, our method of 'rocking-curve imaging' (alias 'area diffractometry') (Lübbert et al., 2000) realises spatial resolution not on the incident-, but on the exit-beam side. It has been applied to determine the crystalline quality in various semiconductor materials (Lübbert et al., 2000) as well as in synthetic diamond samples (Hoszowska et al., 2001) and has recently been extended to allow simultaneous determination of lattice misorientations in all three angular directions (Mikulík et al., 2003).

A related method, referred to as 'MAXIM', has been developed independently by Wroblewski et al. (1995, 2000). It also uses spatial resolution in the exit beam, with an additional microchannel-plate placed between sample and detector as a collimating element. In this way, a second dimension in angular (reciprocal) space can be scanned, and lattice parameter differences in highly strained samples and/or phase coexistence be detected, at the expense of more complicated instrumentation and larger amounts of data to be processed. This method thus specializes on more highly disturbed systems, polycrystals and powders, while our RCI technique is ideal for moderately perfect (single) crystals, such as semiconductor wafers, the imperfections of which are to be investigated with very high spatial and angular resolution.

In this article, we present a new extension and methodical improvement of the rocking-curve imaging technique, which now also allows the quantitative determination of net dislocation densities in the sample surface plane *via* their signature in terms of local lattice curvature. The validity of the method will be demonstrated with examples of an InP and a GaAs wafer, and the merits and limitations of the new procedure will be discussed in detail.

2. Experiment

The experiments were performed on two different compound semiconductor substrate wafers, each of 5 cm diameter. The first, a Czochralski-grown InP (001) wafer doped with sulfur at a concentration of 6×10^{18} cm^{-3}, was expected to be of very good crystalline quality. A zero dislocation density was predicted in the main part of the wafer, with only some dislocations close to the wafer edges, as verified by classical topography on X-ray film. This sample was selected as a reference in order to test and validate the method. The second sample was a semi-insulating undoped Czochralski-grown GaAs (001) wafer. Samples of this kind are known to have a higher dislocation density, of the order of 10^4–10^5 cm^{-2}, typically distributed in a W-shaped pattern (high dislocation density in the centre and along the wafer edges, lower density between).

The X-ray diffraction experiments were performed at the ID19 beamline of the ESRF, Grenoble (France). The X-ray beam from the wiggler source was monochromated by a vertically diffracting Si-111 double-crystal monochromator to a photon energy of 9 keV (λ = 1.37 Å). The beam was then directed onto the wafer sample, which was set to the diffraction position for the 004 reflection in a horizontal scattering plane (σ–π geometry). Bragg angles for this reflection were 27.99° for InP and 29.17° for GaAs. The crucial advantage of this beamline is the very long source-to-sample distance of 145 m; this allows one to obtain a wide beam (15 × 40 mm) while not compromising the very low angular divergence. Thus, the entire sample area could be covered in just four vertical slices, while the lateral dimensions of the sample easily fit into the beam width due to the effect of lateral projection by the Bragg angle.

The diffracted beam profile was recorded by a digital FReLoN CCD camera (Labiche et al., 1996) with 1024^2 pixels. The camera was set reasonably close to the sample (distance 15 cm); a coarse pixel size of 40 μm was used, thus obtaining a maximum field of view of 4 × 4 cm. The lateral spatial resolution is basically determined by the pixel size, with 'lateral' being defined perpendicular to the exit beam. On the sample surface one has additionally to take into account the back-projection of the pixel on the surface plane, and the mean information depth. The latter is determined by the absorption length and, more importantly for rather perfect crystals, by the extinction length of X-rays in the material. A sketch of the entire experimental geometry is shown in Fig. 1.

After adjusting the sample and camera positions to the reflection positions, the sample was rotated around the vertical axis in very small angular steps (0.0005°) over a total range of up to 0.20°. A CCD image of the intensity distribution in the diffracted beam (a digital X-ray topograph) was recorded at each individual angular position, and the entire series of topographs stored on a computer. The sample was then vertically translated and the procedure repeated until the entire wafer surface had been covered.
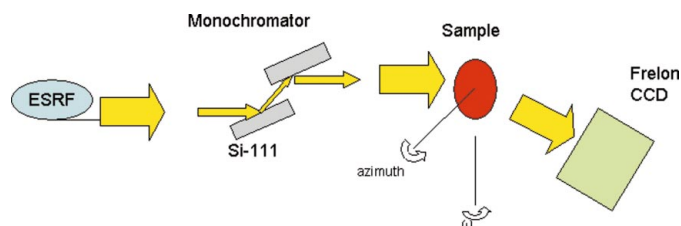

Figure 1
Geometry of a rocking-curve imaging (RCI) measurement: a wide parallel X-ray beam from the wiggler source is monochromated by a vertically diffracting two-crystal Si-111 monochromator. After horizontal diffraction by the sample, the signal is detected by a CCD camera placed at the scattering angle 2θ with respect to the incident beam.

In a second step, the sample was rotated by $90°$ around its surface normal, and the entire measurement repeated. In this way, lattice tilts of the (004) planes along two perpendicular directions could be measured across the entire wafer area.

3. Data analysis

The initial stage of data analysis followed the principles described by Lübbert et al. (2000): the series of digital topographs recorded along the rocking curve of the sample can alternatively be viewed as thousands of local rocking curves recorded simultaneously in parallel. The data were therefore reorganized in order to extract curves of diffracted intensity versus rocking angle for each individual image pixel. The shape of these 'local rocking curves' was then analyzed in terms of peak height, peak width (FWHM) and angular peak position, and the resulting values plotted as spatial distributions (maps).

In our previous investigations, the map of FWHM values was used as an indicator of crystalline quality. In what follows, we take a new approach by focusing exclusively on the maps of angular Bragg peak position, and analyzing them in terms of specific local changes of lattice curvature. These can then be interpreted as a typical signature of dislocations, thus allowing their density to be quantified.

Generally, a change in Bragg angle θ_B can be caused by either lattice tilts $\Delta\varphi$ or lattice parameter variations $\Delta d/d$, according to the equation

$$\Delta\theta_B = -\tan\theta_B (\Delta d/d) \pm \Delta\varphi. \tag{1}$$

The relative importance of both contributions was analyzed by recording and evaluating the rocking-curve imaging series twice, in 0 and $180°$ azimuth (rotation around the sample surface normal). The average and the difference of both measurements yield the lattice parameter variation and lattice tilts, respectively. The results confirmed that the effect of lattice parameter variations is negligible in our case (below 10^{-4}).

This fact supports our interpretation of spatial resolution being directly related to pixel size. Larger lattice parameter variations in the sample would lead to differences in scattering angles, which translate into lateral shifts Δx in the detector plane according to

$$\Delta x = 2D\Delta\theta = 2D\tan\theta (\Delta d/d),$$

where D is the sample–detector distance. For our conditions, the lateral shift is below one detector pixel provided that strain variations are lower than $\Delta d/d = 4.8 \times 10^{-4}$.

Another kind of image blurring (along the vertical direction) can be caused by rather large two-dimensional tilts of single crystallites. Their effect can be understood and analyzed as shown by Mikulík et al. (2003).

In order to obtain precise values for the angular peak positions representative of the real lattice tilts in the sample, the measured maps were corrected for instrumental effects. In fact, the dispersive arrangement of monochromator and sample with perpendicular diffraction planes causes only a narrow band across the sample surface to be in diffraction position simultaneously. An artificial diagonal gradient is thus visible in the experimental peak position maps. Based on a mathematical description of the beamline geometry (Servidori et al., 2001), this effect can be calculated and subtracted from the experimental data. The final maps shown below were all corrected in this way, and are therefore representative of the real lattice curvature in the sample.

Four slices measured in this way were stacked vertically and overlaid on each other to recover a combined map of the entire wafer surface. To facilitate the procedure, it was made sure in the measurement that adjacent slices overlap in a certain region at the edges. A smooth and continuous fitting of the external sample shape was used as a criterion for successful overlaying. As a potential alternative, the matching of visible internal defects could be used in the more difficult cases of less characteristic external sample shapes or incomplete illumination of a (larger) sample area.

In addition to the spatial matching, adjacent slices also need to be made to coincide in angle. In fact, raw maps of angular Bragg peak position show sharp discontinuities across the edges, with angular jumps on the order of some $0.01°$. This was ascribed to a slight rotational instability of the translation stage, and was compensated by shifting each individual map by a fixed angular offset. The spatial overlap regions were again essential in order to determine best fit values for these offsets. Nevertheless, a small remaining discontinuity across the edges is still apparent in the corrected maps (Figs. 2 and 3). This may be due to yet another mechanical instability, a slight involuntary sample tilt upon translation, and could not be compensated. Although this is unpleasant, it does affect a single row or column of image pixels only, and in no way perturbs the main part of the sample area.

The second map of angular peak positions (Fig. 3), measured in the $90°$ azimuth position, represents the local lattice tilts along a direction perpendicular to the first. In order to achieve pixel-wise matching of the two combined images, two more processing steps were performed: first, the second image was rotated back by $-90°$. Then, both images were stretched to make their spatial resolutions match: in fact, the image of the sample is compressed in the horizontal diffraction plane by a factor $\sin\theta_B$, where the value of the Bragg angle θ_B is close to $30°$ in our case. Therefore, the camera pixel size of $(40\,\mu m)^2$ corresponds to a resolution in the sample plane of $40\,\mu m$ vertically by nearly $80\,\mu m$ horizontally in the first map, and vice versa for the back-rotated second map. This projection effect was undone by stretching both images in the respective direction. Finally, the resulting images were interpolated to a common square grid of $(80\,\mu m)^2$ pixel size.

Dislocation densities were calculated from the measured tilt maps in the following way (Ferrari et al., 1997). Consider the lattice displacement field $\mathbf{u}(\mathbf{r})$. We focus on its component along the direction of surface normal $u_z(x, y)$ as a function of position (x, y) in the plane of the sample surface. The measured tilts θ_x, θ_y along the two in-plane axes are related to its gradient via
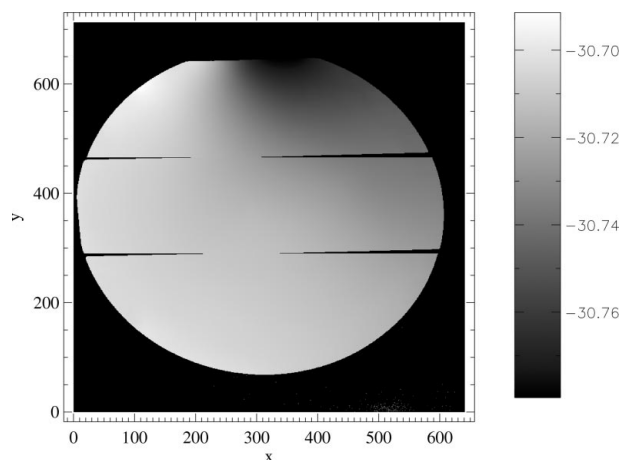
Figure 2
A map of angular Bragg peak positions (°), measured at the 004 reflection of an InP sample. Axes are in units of pixels of 80 µm.
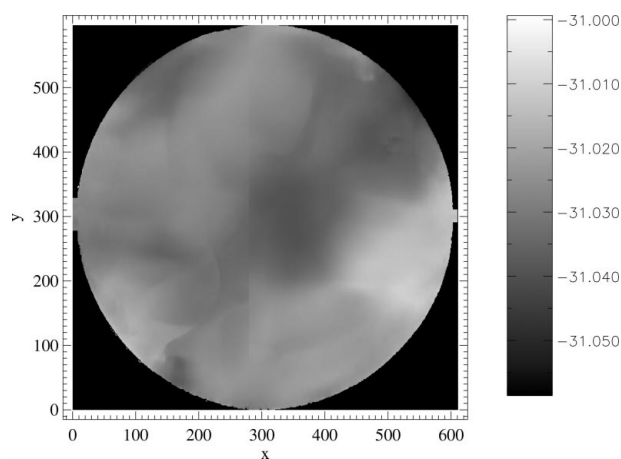

Figure 3
A map of angular Bragg peak positions (°), measured at the 004 reflection of a GaAs sample. Axes are in units of pixels of 80 µm.

$$\theta_x(x, y) = -\frac{\partial u_z(x, y)}{\partial x} \tag{2}$$

and

$$\theta_y(x, y) = -\frac{\partial u_z(x, y)}{\partial y}. \tag{3}$$

We define a new two-dimensional vector field **H** as

$$\mathbf{H}(x, y) = \left[\theta_x(x, y), \theta_y(x, y)\right]. \tag{4}$$

It is then easy to see that $\mathbf{H}(x, y)$ is identical to the two-dimensional gradient of $u_z(x, y)$ in the surface plane:

$$\mathbf{H}(x, y) = -\nabla u_z(x, y). \tag{5}$$

Consider the integral of **H** along a closed path around some point on the sample surface. In a perfect crystal, the integral is zero everywhere. In a crystal containing dislocations, however, we have (Hirth & Lothe, 1982)

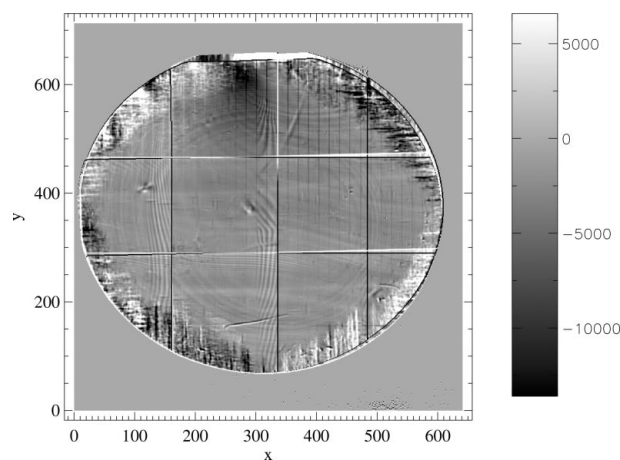$$-\oint_A \mathbf{H}\,d\mathbf{r} = \Delta u_z^A = \sum_{i \in A} b_z^i. \tag{6}$$

Figure 4
Map of dislocation densities (cm^{-2}) in the InP sample. Axes are in units of pixels of 80 µm.

The residual displacement Δu_z is thus equal to the sum of z components of the Burgers vectors **b** of all dislocations i that cross the sample surface inside the integration area A.

By using Stoke's theorem, we convert the expression from the integral into the differential form, which is more suitable for treatment by discrete digital image analysis:

$$-\nabla \times \mathbf{H}(x, y) = \frac{\partial \theta_x(x, y)}{\partial y} - \frac{\partial \theta_y(x, y)}{\partial x} = \frac{1}{A}\sum_i b_z^i. \tag{7}$$

In other words, by applying the curl (rot) operator to **H**, we obtain for each pixel the sum of Burgers vector components of dislocations crossing the sample surface inside the area of the respective pixel, divided by the pixel area. In practice, this curl operator can be simply calculated by taking the difference of the appropriate spatial derivatives of the two experimentally measured tilt maps. The resulting Burgers vector component density can finally be converted into the number density of dislocations ρ by defining an average z component $|b_z|$ of a single dislocation:

$$\rho(x, y) = \frac{1}{A|b_z|}\sum_i b_z^i. \tag{8}$$

Typical dislocations in compound semiconductors with a face-centred cubic (f.c.c.) lattice are of the $\mathbf{b} = a/2\,\langle 011\rangle$ type (Hull & Bacon, 2001), leading to values of $|b_z| = a/2 = 2.934$ Å for InP and 2.827 Å for GaAs.

4. Results and discussion

The resulting map of dislocation densities for the InP sample is shown in Fig. 4. Before discussing the merits of this figure, let us briefly clarify the origins of some obvious artefacts. The most prominent ones are a set of sharp lines at the interfaces between the individual slices that were combined to form the overall image. As mentioned above, these discontinuities are due to the imperfect matching of the Bragg peak position maps on both sides of the respective contact line, and their effect is limited to a single row or column of pixels. Similar, but weaker linear artefacts are visible in the upper centre-right of

the image. In the lower centre-left, two separate regions with wave-like patterns are visible. The origin of the latter two effects is still unclear and must be left open.

Apart from these imperfections, the image beautifully confirms the expectations from crystal growth: the dislocation density in large areas of the centre of the sample is very close to zero, indicating a very perfect crystal. The absolute values in the few more disturbed regions are on the order of 10^4 cm^{-2}: very close to expectations. Apart from one more highly disturbed region in the lower centre, high levels of dislocation density occur mainly in the four diagonal directions, with high positive densities in the upper left and lower right, and high negative values in the other two directions. Considering that the wafer flat at the top indicates a [110] direction, these diagonals are easily identified as ⟨100⟩ types of directions. Dislocations thus pile up at the wafer extremities along high-symmetry directions. Looking more closely, one notices that the zones of highest densities run along horizontal or vertical lines. These are interpreted as dislocation bundles concentrated along ⟨110⟩ types of directions. Both effects are similar to the observations by 'classical' X-ray topography of dislocation bundles in GaAs wafer made by Möck (2001). In the present context, they can be explained in terms of dislocation slip along ⟨110⟩ directions parallel to the wafer surface, which correspond to the traces of easy glide (111) planes for f.c.c. crystals on the (001) surface on the sample. The driving force for the introduction of such dislocations during crystal growth or cooling is the radial stress due to the temperature gradient from the core to the surface of the ingot and the higher value of the Schmid factor [the resolved shear stress along easy glide directions (Hull & Bacon, 2001)] at the ⟨100⟩ edges of the wafer.

The results from the InP sample thus demonstrate the validity of our method: both the absolute values of dislocation densities and their spatial distribution closely match the expectations for this reference sample. The results for the second sample, the GaAs wafer, are shown in Fig. 5. Apart from the same kind of linear artefacts along the 'seams' as
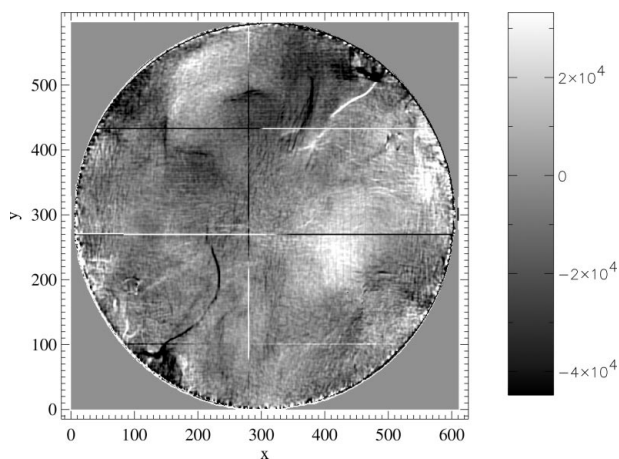
above, the map displays an overall higher level of dislocation densities, of the order of 2–3×10^4 cm^{-2}. This indicates a less perfect crystalline quality, and is again in the range expected from crystal growth (10^4–10^5 cm^{-2}). The spatial distribution, on the other hand, less closely matches expectations: apart from a number of extended regions with higher dislocation densities, the distribution is rather inhomogeneous, and the expected W-shaped profile is not obvious. However, a cellular structure and lineages, as well as a roughly fourfold rotational symmetry of the dislocation density distribution, are present also in this sample.

When interpreting the results, a few features of the method need to be kept in mind. Firstly, density values can be both positive and negative, with the sign indicating the relative orientation of the Burgers vector (parallel or antiparallel to the diffraction vector **Q**). Thus, the results do not represent absolute dislocation densities, but rather an effective density describing the net difference between dislocations with the two opposite orientations. In particular, a value of zero does not necessarily indicate a complete absence of dislocations, but may as well mean that the contributions from the two orientations are balanced and cancel each other. Therefore, the results potentially depend on the spatial resolution of the measurement. Resolution can be enhanced below the value used in the present study simply by choosing a smaller detector pixel size. This will work well down to a few micrometres, at which scale the finite scattering volume (finite information depth of X-rays from the sample, as given by the primary extinction and absorption lengths, of the order of 1–2 μm for our experimental conditions), seen from two different azimuths, limits the achievable resolution also in the lateral plane.

Secondly, our method is selectively sensitive to a certain type of dislocations only: those fulfilling the conditions that (a) their dislocation line crosses the sample surface and (b) their Burgers vector has a component along the scattering vector. This is particularly true for screw dislocations crossing the surface, but equally well for some edge dislocations. Inversely, we are not sensitive to any dislocations running parallel to (below) the surface, nor do we detect those with a Burgers vector parallel to the sample surface. To monitor the latter, one could perform a second measurement in Laue (transmission) geometry, such as in the work of Lübbert et al. (2000), using e.g. a 220 reflection.

5. Conclusion

To conclude, we have demonstrated how the technique of rocking-curve imaging, developed previously to visualize the crystalline quality and the grain structure of a sample, can be extended to quantify effective densities of dislocations. These are characterized by the density of dislocation Burgers vector components along the scattering vector. A more complete three-dimensional Burgers vector analysis is possible by carrying out similar measurements on a full set of three orthogonal reflections. A great advantage over scanning techniques is that this method does not require any sophisti-

Figure 5
Map of dislocation densities (cm^{-2}) in the GaAs sample. Note the higher densities and the less homogeneous distribution of dislocations than in the case of the InP sample. Axes are in units of pixels of 80 μm.

cated X-ray optics. While the spatial resolution in a first experiment was chosen to be moderately low (80 µm), a future extension to length scales of a few micrometres (depending on primary extinction and absorption lengths) only requires a smaller detector pixel size, and correspondingly longer counting times. The analysis of our experimental data showed that the measured shifts in Bragg peak positions were almost exclusively due to lattice tilts, and that lattice parameter variations were negligibly small. The distribution of dislocation Burgers vector densities extracted from the experimental data was clearly non-uniform for both the InP and the GaAs sample. These results demonstrate that the rocking-curve imaging method is a reliable alternative to traditional ways of measuring dislocation densities, and can be applied to large-scale crystals. Apart from its non-destructive character, the main new feature of our method is that it can distinguish between oppositely oriented dislocations, which is not the case for the more classical methods like etch pit measurements or 'simple' X-ray topography. In other words, it investigates not simply the dislocation density, but also the Burgers vector distribution. This might provide valuable experimental input for further developing numerical models of dislocation evolution during crystal growth.

The method can be applied not only to bulk semiconductor wafers, but in fact to any kind of single-crystalline structure, as long as they display moderately low values of lattice imperfections. Due to the non-destructive character of the method, applications to entire microelectronic and/or optoelectronic devices appear particularly attractive. Opportunities for studies of lattice strain or dislocation evolution during crystal growth or other technological processes are obvious. In fact, investigations *e.g.* on the dislocation generation in semiconductor lasers under operating conditions, such as those conducted with different methods by Zeimer *et al.* (1999), will profit greatly from the speed and spatial resolution achievable with the rocking-curve imaging technique, and are already under way.

References

Authier, A. (2001). *Dynamical Theory of X-ray Diffraction*, *International Union of Crystallography Monographs on Crystallography*, Vol. 11. Oxford University Press.

Berg, W. F. (1931). *Naturwissenschaften*, **19**, 391–396.

Bowen, D. K. & Tanner, B. K. (1998). *High Resolution X-ray Diffractometry and Topography*. London: Taylor and Francis.

Castelnau, O., Drakopoulos, M., Schroer, C., Snigireva, I., Snigirev, A. & Ungar, T. (2001). *Nucl. Instrum. Methods A*, **467–468**, 1245–1248.

Chikaura, Y. & Suzuki, Y. (1993). *J. Appl. Cryst.* **26**, 219–225.

DuMond, J. W. (1937). *Phys. Rev.* **52**, 872–883.

Ferrari, C., Korytár, D. & Kumar, J. (1997). *Il Nuovo Cimento*, **19D**(2–4), 165–173.

Goorsky, M. S., Matney, K., Meshkinpour, M., Streit, D. C. & Block, T. R. (1997). *Il Nuovo Cimento*, **19D**(2–4), 257–266.

Hirth, J. P. & Lothe, J. (1982). *Theory of Dislocations*. New York: John Wiley.

Hoszowska, J., Freund, A. K., Boller, E., Sellschop, J. P. F., Level, G., Härtwig, J., Burns, R. C., Rebak, M. & Baruchel, J. (2001). *J. Phys. D Appl. Phys.* **34**, A47–A51.

Hull, D. & Bacon, D. J. (2001). *Introduction to Dislocations*, 4th ed. Oxford: Butterworth/Heinemann.

Köhler, R. (1993). *Röntgenkristalloptik: Topographie und Diffraktometrie mit ebenen Wellen*, Habilitation thesis, Humboldt-Universität Berlin.

Labiche, J.-C., Segura-Puchades, J., van Brussel, D. & Moy, J. P. (1996). *ESRF Newslett.* **25**, 41–43.

Lang, A. R. (1959). *Acta Cryst.* **12**, 249–250.

Larson, B. C., Yang, W., Ice, G. E., Budai, J. D. & Tischler, J. Z. (2002). *Nature (London)*, **415**, 887–890.

Lübbert, D., Baumbach, T., Härtwig, J., Boller, E. & Pernot, E. (2000). *Nucl. Instrum. Methods B*, **160**, 521–527.

Mikulík, P., Lübbert, D., Korytár, D., Pernot, P. & Baumbach, T. (2003). *J. Phys. D Appl. Phys.* **36**, A74–A78.

Möck, P. (2001). *J. Appl. Cryst.* **34**, 65–75.

Poulsen, H. F., Nielsen, S. F., Lauridsen, E. M., Schmidt, S., Suter, R. M., Lienert, U., Margulies, L., Lorentzen, T. & Juul Jensen, D. (2001). *J. Appl. Cryst.* **34**, 751–756.

Poulsen, H. F. & Schmidt, S. (2003). *J. Appl. Cryst.* **36**, 319–325.

Servidori, M., Cembali, F. & Milita, S. (2001). *Appl. Phys. A*, **73**, 75–82.

Tamura, N., MacDowell, A. A., Spolenak, R., Valek, B. C., Bravman, J. C., Brown, W. L., Celestre, R. S., Padmore, H. A., Batterman, B. W. & Patel, J. R. (2003). *J. Synchrotron Rad.* **10**, 137–143.

Wroblewski, T., Almanstotter, J., Clauss, O., Moneke, M., Pirling, T. & Schade, P. (2000). *Mater. Sci. Eng. A*, **288**, 126–131.

Wroblewski, T., Geier, S., Hessmer, R., Schreck, M. & Rauschenbach, B. (1995). *Rev. Sci. Instrum.* **66**, 3560–3562.

Zachariasen, W. H. (1945). *Theory of X-ray Diffraction in Crystals*. New York: John Wiley.

Zeimer, U., Baumbach, T., Grenzer, J., Lübbert, D., Mazuelas, A., Pietsch, U. & Erbert, G. (1999). *J. Phys. D Appl. Phys.* **32**, A123–A127.